

Ultrahigh accuracy imaging modality for super-localization microscopy

Jerry Chao¹⁻³, Sripad Ram¹⁻³, E Sally Ward² & Raimund J Ober^{1,2}

Super-localization microscopy encompasses techniques that depend on the accurate localization of individual molecules from generally low-light images. The obtainable localization accuracies, however, are ultimately limited by the image detector's pixelation and noise. We present the ultrahigh accuracy imaging modality (UAIM), which allows users to obtain accuracies approaching the accuracy that is achievable only in the absence of detector pixelation and noise, and which we found can experimentally provide a >200% accuracy improvement over conventional low-light imaging.

Super-localization microscopy¹⁻⁶ comprises an ever-expanding set of techniques that rely on pinpointing the locations of individual fluorescent molecules for purposes such as the high-resolution reconstruction of subcellular structures and high-accuracy tracking of protein movement inside cells. Common to these techniques is the use of a pixelated detector to record the fluorescence signal collected by the microscope and produce images from which the molecules are subsequently localized. The detector is typically a charge-coupled device (CCD) detector or an electron-multiplying CCD (EMCCD) detector⁷. Both types of detectors accumulate photoelectrons in their pixels in proportion to the number of detected photons and produce a digitized image via a readout process. The EMCCD detector, however, has a multiplication register that amplifies the number of photoelectrons before they are read out, with the intended purpose of augmenting weak signals above the readout noise floor.

A key impediment to the localization of a fluorescent molecule with ultrahigh accuracy is the fact that CCD and EMCCD detectors deteriorate the acquired image in two major ways. First, they pixelate the image, thereby substantially lowering its resolution. To improve the localization accuracy in the context of scanning microscopy, for example, an approach⁸ has been described that addresses the issue of pixelation via the detection of single photons. Second, they introduce noise to the image. For the CCD detector,

the primary noise source is the aforementioned readout noise, which overwhelms weak signals and renders the CCD detector unsuitable for extremely low-light imaging. For the EMCCD detector, besides the readout noise, the signal amplification is itself an important noise source because of its stochastic nature. Pixelation and noise can lead to localization accuracies that are substantially lower than the accuracy that is possible if the image were recorded with an ideal detector that captures it exactly as produced by the microscope.

The deteriorative effects of detector pixelation and noise become especially consequential under low-light conditions; even in their absence, the accuracy of localization that can be expected is relatively poor owing to the low numbers of photons that can be detected. This directly follows from the well-known fact that estimation accuracies worsen with decreasing photon count⁹. However, in many practical situations, low photon counts in the acquired data are unavoidable or necessary. In super-resolution microscopy^{3,5,6}, relatively weak fluorophores often need to be chosen because they possess desirable attributes that brighter fluorophores lack. Examples include the preferred use of weak genetically encoded fluorescent proteins for their labeling specificity¹⁰ and the selection of weak dyes in multicolor super-resolution imaging based on, for instance, the necessity of using spectrally well-separated fluorophores. Moreover, in live-cell super-resolution imaging and single-molecule tracking, even the use of bright fluorophores typically results in low-photon-count images owing to the fast acquisition rate that is required to follow the dynamics of the cellular structures and molecules. More generally, to minimize phototoxicity and at the same time maximize the duration over which samples can be imaged¹¹ using the many conventional dyes and fluorescent proteins that have limited photostability, microscopists might even wish to purposely acquire low-photon-count images using low excitation power levels. The extension of imaging time is of particular importance for single-molecule tracking, as then substantially longer trajectories can potentially be observed.

Here we introduce UAIM, a method of low-light imaging that enables localization with much higher accuracy than is permitted by conventional EMCCD imaging. In fact, the accuracy of UAIM can approach that of an ideal noiseless and unpixelated detector used under the same imaging conditions. UAIM uses an EMCCD detector at a high level of signal amplification and in a highly unconventional setting in which the number of photons detected in each pixel of an acquired image generally averages <1 (**Supplementary Notes 1 and 2**). This may seem counterintuitive, as such an image (**Fig. 1a**) does not give a visually clear representation of the object of interest, such as one would expect would be required for obtaining high localization accuracies.

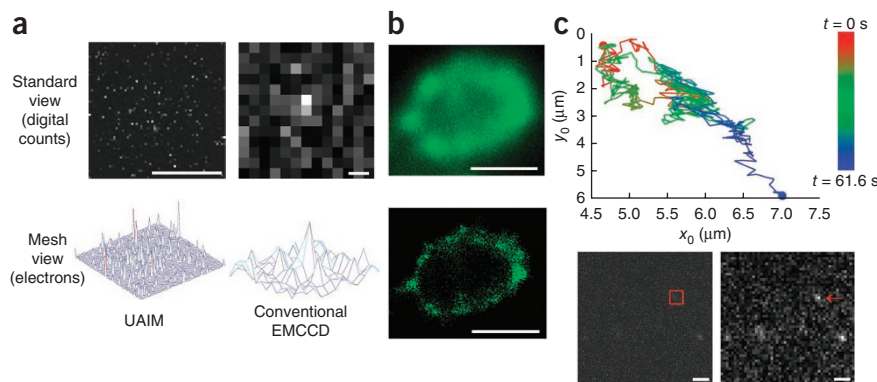
¹Department of Electrical Engineering, University of Texas at Dallas, Richardson, Texas, USA. ²Department of Immunology, University of Texas Southwestern Medical Center, Dallas, Texas, USA. ³These authors contributed equally to this work. Correspondence should be addressed to R.J.O. (ober@utdallas.edu).

Figure 1 | UAIM and its applications.

(a) Visual comparison of a UAIM image and a conventional EMCCD image. Images are of an Atto 647N molecule from which ~72 (UAIM) and ~84 (conventional) photons per image were detected on average; images were acquired with effective pixel sizes of 16 and 253.97 nm using 1,000× and 63× magnifications, respectively. The mean photon count in the brightest pixel is 0.22 for the UAIM image and 21.85 for the conventional image. The mesh representation, which displays intensity as height, contrasts more conspicuously the spiky appearance of the UAIM image with the relatively smooth appearance of the conventional image. Scale bars, 0.5 μm.

(b) Super-resolution imaging of a LAMP1+ cellular structure using UAIM. Top, image of the structure, formed by summing the 5,063 UAIM (1,000×) images from which single Alexa 647 molecules were localized to produce a super-resolution image. Bottom, super-resolution image constructed from the location estimates of individual Alexa 647 molecules. The average number of photons detected per molecule is 128.94. Scale bars, 1 μm.

(c) Single-molecule tracking using UAIM. Top, trajectory of an ErbB2 receptor (Supplementary Video 1) determined by localization of its Atto 647N label from 594 UAIM (1,000×) images. On average, 102.85 photons per image were detected from the Atto 647N dye. Bottom left, one of the 594 UAIM images. The red box encloses the tracked Atto 647N molecule. Bottom right, compacted (10 × 10–binned) version of the same UAIM image that facilitates visualization of the tracked Atto 647N molecule (red arrow). Scale bars, 1 μm.



We demonstrate with the localization of fluorescent beads that, despite expectations, positional coordinates could be estimated with ultrahigh accuracies from such an image using the maximum-likelihood estimator for EMCCD data (Online Methods). We performed super-resolution imaging and reconstruction of an Alexa 647–labeled LAMP1+ cellular structure (Fig. 1b), for

which 128.94 photons on average—a relatively low number—were detected per dye molecule. Finally, we tracked the plasma membrane dynamics (Fig. 1c and Supplementary Video 1) of an ErbB2 receptor over an interval of just over 60 s, for which an average of 102.85 photons per image were detected from the Atto 647N dye used to label the receptor.

To demonstrate the substantial advantage that UAIM has over conventional EMCCD imaging in terms of localization accuracy, we took images of stationary 50-nm fluorescent beads using a microscope equipped with an EMCCD camera and used maximum-likelihood estimation to determine bead positions from both UAIM and conventional EMCCD images containing on average <200 bead photons. The s.d. values of the resulting estimates of the x_0 positional coordinate of different beads are plotted in Figure 2a. Shown as a function of the mean photon counts detected per image from the beads, the s.d. are clearly separated into a lower group that represents very high accuracies and corresponds to

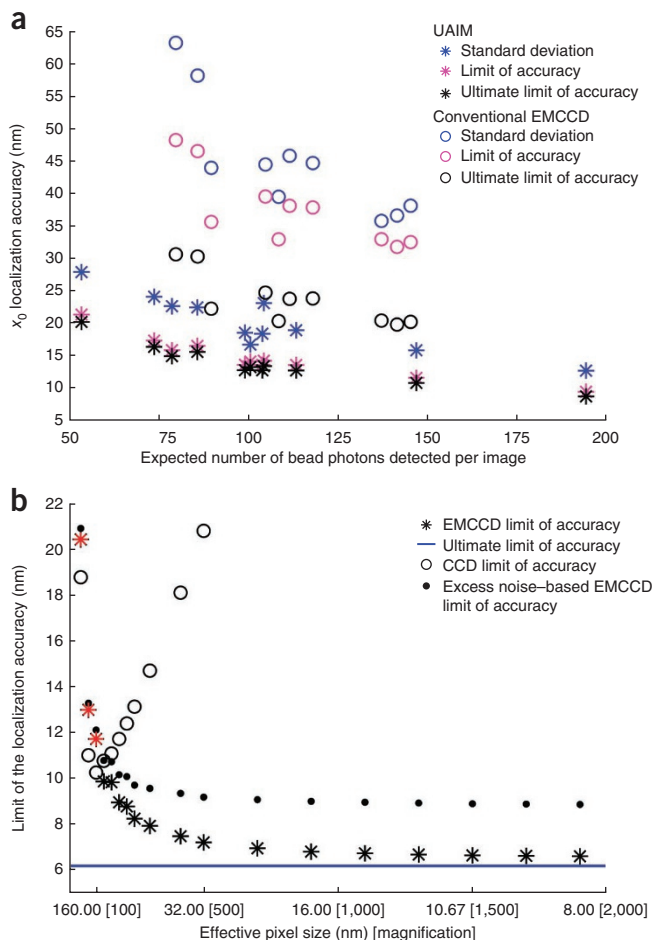


Figure 2 | Experimental and theoretical demonstration of UAIM.

(a) Comparison of the s.d. of the maximum-likelihood estimates of the x_0 coordinate of fluorescent beads imaged using UAIM (blue stars) and conventional EMCCD imaging (blue circles). Each s.d. corresponds to a different bead that is identified by its per-image mean photon count. For each s.d., the corresponding limit of accuracy (magenta) is shown. Likewise, the corresponding ultimate limit of accuracy (black), which assumes an ideal detector that introduces neither noise nor pixelation, is shown. The UAIM and conventional images were acquired with effective pixel sizes of 16 and 253.97 nm using 1,000× and 63× magnifications, respectively. (b) Theoretical analysis of point-source localization. Decreasing the effective pixel size by increasing the magnification for EMCCD imaging at a high level of signal amplification ($g = 1,000$) yields a limit of accuracy (stars) that approaches the ultimate limit (blue line). The red markers at effective pixel sizes of 373.31, 224.00 and 160.00 nm (magnifications of $M = 42.86, 71.43$ and 100) correspond approximately to standard magnifications of 40× and 63× and exactly to the standard magnification of 100×. For the same range of effective pixel sizes, the limits of accuracy corresponding to the common excess noise–based supposition (dots) and to CCD imaging with a readout noise s.d. of two electrons per pixel (circles) are shown. (See Supplementary Note 9 for more details.)

Table 1 | Results of maximum-likelihood estimation with simulated data

| Imaging scenario | True value of both x_0 and y_0 (nm) | Mean of x_0, y_0 estimates (nm) | Limit of accuracy for both x_0 and y_0 (nm) | s.d. of x_0, y_0 estimates (nm) |
|--------------------|---|-----------------------------------|---|-----------------------------------|
| Ideal | 0 | 0.00, 0.00 | 6.19 | 6.29, 6.32 |
| Conventional EMCCD | 560 | 560.02, 559.80 | 11.72 | 11.71, 12.01 |
| UAIM | 560 | 559.90, 560.53 | 6.81 | 7.04, 6.83 |

Maximum-likelihood estimation was used to localize a point source from images simulated according to the ideal, conventional EMCCD and UAIM imaging scenarios. Note that the single limit of accuracy shown per scenario applies to the estimation of both x_0 and y_0 because the image of the point source was simulated to be exactly centered on a square region. See **Supplementary Note 12** for the simulation parameters.

the beads imaged with UAIM and a higher group that represents substantially poorer accuracies and corresponds to the conventionally imaged beads. The s.d. for the beads imaged with UAIM ranged from 27.87 to 12.70 nm over a per-image mean photon count range of 53.34–194.06, corresponding to a more than two-fold improvement over the s.d. for the conventionally imaged beads, which ranged from 63.11 to 38.07 nm over a per-image mean photon count range of 79.64–145.13.

For both UAIM and conventional EMCCD imaging, we compared each s.d. of x_0 estimates to the corresponding theoretical best possible s.d., or limit of accuracy (**Supplementary Note 3**), and to the corresponding ultimate limit of accuracy (**Supplementary Note 4**), which assumes an ideal detector. In both cases, the s.d. were reasonably close to their respective limits of accuracy, but only in the case of UAIM were these limits in turn very close to their corresponding ultimate limits (**Fig. 2a**). UAIM therefore allowed estimation with s.d. that approached the values one can achieve only with an ideal detector. (For similar results obtained for the localization of stationary single molecules, see **Supplementary Table 1** and **Supplementary Note 5**.)

We confirmed our experimental results by carrying out maximum-likelihood estimations on simulated images of a point source. The results obtained for an ideal, a conventional EMCCD and a UAIM data set, each consisting of images of the same point source, are summarized in **Table 1**. Besides affirming that UAIM enables estimation with accuracies close to the ultimate limit, these simulation results suggest that the maximum-likelihood estimator is capable of attaining the limit of accuracy in all cases.

UAIM's stipulation of reducing the signal level per pixel is based on theoretical analyses that utilize our careful modeling¹² of the EMCCD signal amplification process. These analyses indicate that under the regime in which each EMCCD pixel generally detects fewer than one photon on average, detector noise is minimized and an image is produced that enables estimation of the quantity of interest with nearly as high an accuracy as would an image that is free of detector noise (**Supplementary Note 6**). This regime was achieved here by decreasing the effective pixel size of the detector via the use of a magnification about an order of magnitude higher (1,000 \times for bead images, 900 \times for simulated images) than what is typical, thereby distributing the detected photons over many more pixels of the detector. This approach not only minimizes the detector noise by virtue of the signal reduction per pixel but also generates a much more finely pixelated image of considerably higher resolution that more closely approximates an ideal image. By substantially reducing both major deteriorative effects of the detector, this implementation yields estimation accuracies that nearly attain the ultimate limit of accuracy. To avoid the reduced field of view (**Supplementary Note 7**) that results

from the use of high magnification, one might alternatively image with a standard magnification but using a nonstandard EMCCD detector with unconventionally small pixels. (See **Supplementary Note 8** for an altogether different approach to realizing UAIM.)

Summarizing the results of a theoretical analysis of our implementation of UAIM (**Fig. 2b** and **Supplementary Note 9**), we see that as the effective pixel size is decreased,

the limit of the accuracy for estimating the positional coordinate of a point source improves and approaches the ultimate limit. At an effective pixel size of just 14.55 nm (1,100 \times magnification), for example, UAIM yields a best possible accuracy of 6.74 nm, which is within 1 nm of the ultimate limit of 6.19 nm. In contrast, conventional EMCCD imaging at an effective pixel size of 160 nm (100 \times magnification), which is within the recommended size range⁶ for fluorescence super-resolution imaging, yields a best possible accuracy of 11.72 nm, nearly double the ultimate limit.

According to the common assertion¹³ based on the signal amplification excess noise^{14–16}, the best estimation accuracy achievable with an EMCCD detector is worse, by a factor of $\sqrt{2}$, than that attainable with a hypothetical noiseless but pixelated detector. Our analysis (**Fig. 2b**) reveals a more complex picture, demonstrating that the $\sqrt{2}$ factor indeed approximates the EMCCD limit of accuracy well at large effective pixel sizes (standard magnifications), when the mean photon count per pixel is relatively high. However, at small effective pixel sizes (high magnifications), when the mean photon count per pixel is extremely low, the $\sqrt{2}$ factor considerably underestimates the attainable accuracy, which in fact approaches the ultimate limit.

A CCD detector, even one with a low readout noise level, is unsuitable for implementing UAIM (**Fig. 2b**). For such a detector, the limits of accuracy are no better than ~ 10 nm for effective pixel sizes between 400 and 160 nm (standard magnifications between 40 \times and 100 \times) and deteriorate quickly as the effective pixel size is decreased. This is due to the detected photons being overwhelmed by readout noise as their numbers in each pixel decrease with the pixel size reduction. As we explain in **Supplementary Note 10**, the same result (**Supplementary Fig. 1**) can be expected for the scientific complementary metal-oxide semiconductor (sCMOS) detector.

We have demonstrated UAIM for image data with relatively low photon counts, but the principle of increasing the estimation accuracy by reducing the photon count in each pixel is applicable to a broad range of photon budgets (**Supplementary Table 2** and **Supplementary Note 11**). In addition, though we have applied UAIM to super-localization microscopy, it is a general imaging method that can be of benefit in other applications (such as astronomy¹⁷ and computer vision¹⁸) in which quantities (not limited to the positional coordinates of objects) need to be extracted from the acquired images. Notably, the fundamental nature of UAIM is such that it can in principle be incorporated into existing imaging techniques to potentially substantially improve the obtainable accuracies.

METHODS

Methods and any associated references are available in the [online version of the paper](#).

Note: Supplementary information is available in the [online version of the paper](#).

ACKNOWLEDGMENTS

This work was supported in part by grant R01 GM085575 from the US National Institutes of Health and in part by the Cancer Prevention and Research Institute of Texas. We thank D. Kim and S. You for their assistance with data analysis.

AUTHOR CONTRIBUTIONS

J.C., S.R. and R.J.O. conceived the experiments, designed the experiments and analyzed the data. J.C. and S.R. performed the experiments. E.S.W. and R.J.O. provided the experimental materials and computing resources. All authors wrote the manuscript.

COMPETING FINANCIAL INTERESTS

The authors declare no competing financial interests.

Reprints and permissions information is available online at <http://www.nature.com/reprints/index.html>.

- Thompson, M.A., Lew, M.D. & Moerner, W.E. *Annu. Rev. Biophys.* **41**, 321–342 (2012).
- Lidke, K.A., Rieger, B., Jovin, T.M. & Heintzmann, R. *Opt. Express* **13**, 7052–7062 (2005).
- Betzig, E. *et al. Science* **313**, 1642–1645 (2006).
- Ram, S., Prabhat, P., Chao, J., Ward, E.S. & Ober, R.J. *Biophys. J.* **95**, 6025–6043 (2008).
- Pavani, S.R.P. *et al. Proc. Natl. Acad. Sci. USA* **106**, 2995–2999 (2009).
- van de Linde, S. *et al. Nat. Protoc.* **6**, 991–1009 (2011).
- Hynecek, J. *IEEE Trans. Electron Devices* **48**, 2238–2241 (2001).
- Larkin, J.D., Publicover, N.G. & Sutko, J.L. *J. Microsc.* **241**, 54–68 (2011).
- Ober, R.J., Ram, S. & Ward, E.S. *Biophys. J.* **86**, 1185–1200 (2004).
- Patterson, G.H. *J. Microsc.* **243**, 1–7 (2011).
- Carlton, P.M. *et al. Proc. Natl. Acad. Sci. USA* **107**, 16016–16022 (2010).
- Chao, J., Ward, E.S. & Ober, R.J. *Multidimens. Syst. Signal Process.* **23**, 349–379 (2012).
- Mortensen, K.I., Churchman, L.S., Spudich, J.A. & Flyvbjerg, H. *Nat. Methods* **7**, 377–381 (2010).
- Matsuo, K., Teich, M.C. & Saleh, B.E.A. *IEEE Trans. Electron Devices* **32**, 2615–2623 (1985).
- Hollenhorst, J.N. *IEEE Trans. Electron Devices* **37**, 781–788 (1990).
- Hynecek, J. & Nishiwaki, T. *IEEE Trans. Electron Devices* **50**, 239–245 (2003).
- Basden, A.G., Haniff, C.A. & Mackay, C.D. *Mon. Not. R. Astron. Soc.* **345**, 985–991 (2003).
- Rohr, K. *J. Math. Imaging Vis.* **7**, 7–22 (1997).

ONLINE METHODS

Microscope setup and image acquisition. All imaging experiments were carried out on a Zeiss Axiovert 200 microscope (Carl Zeiss). The sample was imaged with a Zeiss Plan-Apochromat oil-immersion objective lens (see experiment-specific details below). For UAIM, three Zeiss external Optovars (two 2.5× and one 1.6×) concatenated to achieve a tenfold further magnification were positioned in front of an Andor iXon DU-897 EMCCD camera (Andor Technologies). For conventional EMCCD imaging, the external Optovars were removed. The electron multiplication gain of the camera was set to 950.

For imaging of cell samples, a Zeiss dual video adaptor was installed at the side port of the microscope, which split the emission into two light paths. The external Optovars and the Andor camera were attached to one of the light paths, and a second (i.e., reference) Andor iXon camera was attached to the other light path. The latter camera was used to image fiduciary markers for drift correction, and it also aided in the focusing and scanning of the sample.

For imaging of beads, a 405-nm laser (Opto Engine) was passed through an HQ405/30x cleanup filter (Chroma Technology) and reflected by a 455DCLP dichroic mirror (Chroma) to illuminate the sample, and the resulting fluorescence signal collected by the objective lens (100×/1.4 NA for UAIM (for a total magnification of 1,000×); 63×/1.4 NA for conventional EMCCD imaging) was passed through an HQ480/40m CFP emission filter (Chroma).

For imaging of cells, light from either a 635-nm laser (Opto Engine) or a 488-nm laser (Blue Sky Research) was reflected by a quad-edge dichroic (Di01-R405/488/543/635-25x36; Semrock) to illuminate the sample, and the resulting fluorescence signal was passed through a quad-band emission filter (FF01-446/515/588/700-25; Semrock). Prior to entering the microscope, the 635-nm laser line was passed through a cleanup filter (LD01-640/8-12.5; Semrock) and a quarter-wave plate, and the 488-nm laser line was passed through two cleanup filters (10LF10-488; Newport).

For super-resolution imaging, the cell sample was illuminated with the 635-nm laser. During imaging, the 488-nm laser was turned on either every 76th frame (for LAMP1 imaging) or every 101st frame (for cell membrane imaging) to photoactivate Alexa 647. A 100×/1.4-NA objective lens was used for LAMP1 imaging at a total magnification of 1,000×, and a 63×/1.46-NA objective lens was used for cell membrane imaging at a total magnification of 630×.

For single-molecule tracking and stationary single-molecule imaging, the sample was illuminated with the 635-nm laser. For single-molecule tracking and the UAIM imaging of stationary single molecules, a 100×/1.4-NA objective lens was used to achieve a total magnification of 1,000×. For the conventional EMCCD imaging of stationary single molecules, a 63×/1.4-NA objective lens was used.

The camera acquisition parameters for all imaging experiments are given in **Supplementary Note 13**.

Sample preparation. A bead sample was prepared by adsorbing a dilute solution of 50-nm yellow-green beads (Polysciences) on poly(lysine)-coated glass cover slips. The beads were imaged in ultrapure filtered water.

The super-resolution imaging of LAMP1⁺ structures and of the cell membrane was carried out with HMEC human endothelial

cells¹⁹ and Z310 rat epithelial cells²⁰, respectively. The cells were plated on Zeiss high-performance cover slips, and 1 d before fixation, the cells were pulsed with 100-nm yellow-green beads (Polysciences) to allow internalization of the beads. The beads were used as fiduciary markers for drift correction.

For LAMP1 staining, the sample was fixed with 1.7% (w/v) paraformaldehyde (PFA) and permeabilized with 0.02% (w/v) saponin, each for 10 min at room temperature, and then blocked with 4% BSA (w/v) in PBS, stained with mouse anti-LAMP1 antibody (1:100 dilution; Developmental Studies Hybridoma Bank; clone #H4A3) and counterstained with goat anti-mouse IgG Alexa 647 (1:1,000 dilution; Life Technologies), each for 25 min at room temperature.

For cell membrane staining, Z310 cells were grown to confluence, stained with 1 μg/ml cholera toxin B subunit labeled with Alexa 647 (Life Technologies) for 15 min on ice and then fixed with 1.7% (w/v) PFA for 15 min on ice.

For both types of samples, the medium in the cells was changed to an imaging buffer (PBS, pH 7.4, containing 10% (w/v) glucose; 50 mM 2-mercaptoethylamine; 0.5 mg/ml glucose oxidase and 40 μg/ml catalase) just before the start of imaging.

Live-cell single-molecule tracking experiments and imaging of stationary single molecules were carried out with BT474 human breast cancer epithelial cells. An antibody fragment (Fab) against the human ErbB2 receptor labeled with Atto 647N dye was pulsed at a concentration of 50–270 pM. For tracking experiments, the cell sample was imaged at 37 °C. For the imaging of stationary single molecules, the cell sample was fixed with 1.7% (w/v) PFA for 10 min at room temperature and then imaged at room temperature in PBS containing 1% (w/v) BSA.

Modeling the image of a point source. The image of a point source is assumed to be described by the Airy point-spread function²¹. Expressed in the form of an image function²², which assumes unit magnification and that the point source is located at the origin of the object space in which it resides, it is given by

$$q(x, y) = \frac{J_1^2\left(\frac{2\pi n_a}{\lambda} \sqrt{x^2 + y^2}\right)}{\pi(x^2 + y^2)}, \quad (x, y) \in R^2 \quad (1)$$

where n_a is the numerical aperture of the microscope objective, λ is the wavelength of the detected photons, J_1 is the first-order Bessel function of the first kind and R_n , $n = 1, 2, \dots$, is the n -dimensional Euclidean space.

Image simulation. As is typical, photon detection is modeled as a Poisson process. Therefore, given that, on average, N_{photon} photons per image are detected from a point source over the entire detector plane (i.e., R^2), an ideal image of arbitrarily high resolution with no detector noise is simulated by first generating N_{initial} pairs of x and y coordinates, where N_{initial} is the number of detected photons drawn from the Poisson distribution with mean N_{photon} . Each (x, y) pair represents the location at which a photon is detected, and a pair is generated as random numbers drawn from the probability distribution characterized by the probability density function²²

$$f(x, y) = \frac{1}{M^2} q\left(\frac{x}{M} - x_0, \frac{y}{M} - y_0\right), \quad (x, y) \in R^2 \quad (2)$$

which is just a scaled and shifted version of equation (1) that accounts for the magnification M of the microscope setup and the positional coordinates x_0 and y_0 of the point source in the object space where it resides. Any (x, y) pair that places a photon outside the chosen finite region $C \subset R^2$ occupied by the detector is discarded, leaving N_{pntsrc} pairs of x and y coordinates within C that correspond to photons detected from the point source. The number of background photons (i.e., photons detected from anything other than the point source) in an image is likewise Poisson distributed and is assumed to be independent of the number of photons detected from the point source. Therefore, given that on average β background photons are detected per image, N_{bg} additional (x, y) pairs, where N_{bg} is a number drawn from the Poisson distribution with mean β , are generated. Assuming a uniform background for the image, each background (x, y) pair is generated as random numbers drawn from the spatial distribution characterized by the probability density function $b(x, y) = 1/A$, $(x, y) \in C$, where A is the area of the region C . The simulated ideal image is thus composed of a total of $N_{\text{im}} = N_{\text{pntsrc}} + N_{\text{bg}}$ pairs of x and y coordinates.

To simulate a conventional EMCCD or a UAIM image of K pixels, the mean v_k , $k = 1, 2, \dots, K$, of the Poisson-distributed number of photons detected at the k th pixel is first calculated as

$$v_k = N_{\text{photon}} \int_{C_k} f(x, y) dx dy + \beta_k \quad (3)$$

where N_{photon} and $f(x, y)$ are as defined above, C_k is the region in the detector plane occupied by the pixel, and β_k is the mean number of background photons at the pixel. Given v_k , the eventual value of the k th pixel is then simulated as a random number drawn from the probability distribution characterized by the probability density function¹²

$$p_k(z) = \frac{e^{-v_k}}{\sqrt{2\pi}\sigma_k} \left[e^{-\left(\frac{z-\eta_k}{\sqrt{2}\sigma_k}\right)^2} + \sum_{l=1}^{\infty} e^{-\left(\frac{z-l\eta_k}{\sqrt{2}\sigma_k}\right)^2} \sum_{j=0}^{l-1} \frac{\binom{l-1}{j} \left(1-\frac{1}{g}\right)^{l-j-1}}{(j+1)! \left(\frac{g}{v_k}\right)^{j+1}} \right], \quad z \in R \quad (4)$$

where η_k and σ_k are the mean and s.d. of the Gaussian random variable used to model the EMCCD camera's readout noise at the k th pixel, and g is the signal amplification level (i.e., electron multiplication gain) of the EMCCD camera.

For the parameter values used to simulate the ideal, conventional EMCCD and UAIM data sets of **Table 1**, see **Supplementary Note 12**.

Maximum-likelihood estimation. Given an ideal image consisting of N_{im} photons detected at positions $\{r_j = (x_j, y_j) \in C: j = 1, \dots, N_{\text{im}}\}$, where C is the finite region in the detector plane occupied by the detector, the maximum-likelihood estimation of the x_0 and y_0 coordinates of the point source was carried out by maximizing the log-likelihood function

$$\ln\left(L(x_0, y_0 | r_1, \dots, r_{N_{\text{im}}})\right) = \sum_{j=1}^{N_{\text{im}}} \ln\left(N_{\text{photon}} \times f(r_j) + \frac{\beta}{A}\right) \quad (5)$$

where the probability density function f is given by equation (2), A is the area of the region C , and N_{photon} and β are as defined above.

As indicated by the method of simulation, the value of each pixel of an EMCCD detector is modeled as the sum of an amplified Poisson signal and a Gaussian random variable representing the readout noise. As such, given a conventional EMCCD or a UAIM image of K pixels, be it simulated or experimental, the maximum-likelihood estimation of the x_0 and y_0 coordinates of the point source was carried out by maximizing the log-likelihood function

$$\ln\left(L(x_0, y_0 | z_1, \dots, z_K)\right) = \sum_{k=1}^K \ln(p_k(z_k)) \quad (6)$$

where for $k = 1, \dots, K$, z_k is the value of the k th pixel and p_k is the probability density function given by^{12,13,17}

$$p_k(z) = \frac{e^{-v_k}}{\sqrt{2\pi}\sigma_k} \left[e^{-\left(\frac{z-\eta_k}{\sqrt{2}\sigma_k}\right)^2} + \int_0^{\infty} e^{-\left(\frac{z-u-\eta_k}{\sqrt{2}\sigma_k}\right)^2} \frac{u}{g} \times \frac{\sqrt{v_k u}}{u} I_1\left(2 \times \sqrt{\frac{v_k u}{g}}\right) du \right], \quad z \in R \quad (7)$$

where I_1 is the first-order modified Bessel function of the first kind, and all parameters are as defined above. Instead of equation (4), equation (7) was used for estimation because it can be computed more efficiently and has been demonstrated to be an excellent approximation of equation (4) at high signal amplification levels¹².

Maximization of the log-likelihood functions of equations (5) and (6) was in each case implemented as the minimization of the negative of the log-likelihood function using the "fminunc" function of the MATLAB optimization toolbox (MathWorks). In the analysis of all data sets (simulated and experimental), only the parameters x_0 and y_0 were estimated. All other parameters had fixed values, some of which were first estimated by other means in the case of experimental data (**Supplementary Note 14**). For all data sets, limits of the localization accuracy were computed (**Supplementary Note 15**) either for comparison with the s.d. of the maximum-likelihood estimates of x_0 and y_0 or for characterizing the accuracy with which a representative maximum-likelihood localization was carried out.

Comparison of UAIM and conventional EMCCD imaging.

Fluorescent beads were chosen for our experimental comparison of conventional EMCCD imaging and UAIM for their photostability, which allowed us to obtain the necessary number of repeats of the image of a given bead for determining the localization accuracy. A total of 10 conventional EMCCD (63×) and 11 UAIM (1,000×) data sets were analyzed, each consisting of 951–1,081 images of a single bead. For a given bead, the center of its image was approximately identified by eye, and a square region of interest (ROI) (13 × 13 pixel array for conventional EMCCD, 61 × 61 pixel array for UAIM) was chosen around this center. The selected ROI was extracted from each image of the bead and individually subjected to a maximum-likelihood estimation of the bead's positional coordinates x_0 and y_0 . To correct for drift that was observed during the imaging of the bead, best-fit lines to segments of the x_0 estimates plotted as a function of time were subtracted from the x_0 estimates. The segments were identified on the basis of drift patterns visually observed in the x_0 estimates-versus-time

plot. Independently, the y_0 estimates were piecewise linearly drift-corrected in a similar manner. The s.d. of the drift-corrected x_0 and y_0 estimates were then computed and respectively used as points in the plots of **Figure 2a** and **Supplementary Figure 2**.

The same procedure was followed to compare the two imaging methods using the localization of single molecules. Stationary ErbB2 receptors were imaged with Atto 647N-labeled anti-ErbB2 Fab. From the resulting images, two conventional EMCCD (63 \times) and two UAIM (1,000 \times) data sets were selected, each consisting of between 301 and 403 images of a visually identified, well-isolated Atto 647N molecule. To ensure that a single dye molecule was being observed in each data set, single-step photobleaching was visually verified for the molecule. The images in a data set consisted of a consecutive sequence of frames over which the Atto 647N molecule maintained a relatively stable photon count level, as determined by a plot of the sum of the molecule's ROI pixel values over the frames. The results are presented in **Supplementary Table 1** and discussed in **Supplementary Note 5**.

Super-resolution data analysis. To demonstrate super-resolution imaging with UAIM, two different super-resolution data sets, one of a LAMP1⁺ cellular structure immunofluorescently stained with Alexa 647 and the other of a cell membrane stained with Alexa 647-labeled cholera toxin B subunit, were respectively acquired with a 1,000 \times and a 630 \times magnification and were analyzed as follows. Image frames at which the 488-nm activation laser was turned on were excluded from analysis because they contained a dense distribution of activated Alexa 647 molecules. To further ensure that only images with sparsely distributed activated Alexa 647 molecules were analyzed, an additional 14 and 15 frames immediately following each activation frame were respectively discarded from the LAMP1⁺ cellular structure and cell membrane data sets. To facilitate the identification of Alexa 647 spots, the remaining frames in the data set were compacted by a 10 \times 10 binning of the pixels to produce images that appeared as if they were acquired using a standard magnification that was a factor of 10 lower. Alexa 647 spots in the compacted frames were then identified using a wavelet-based spot detection algorithm²³.

Each identified spot in the compacted frames was represented by a 5 \times 5-pixel ROI that was centered on the spot's brightest pixel. Some of these ROIs were eliminated from further analysis as follows. For selection of only the relatively well-isolated Alexa 647 spots in each image frame for maximum-likelihood localization analysis, ROIs that overlapped with more than one other ROI were discarded. Furthermore, of the remaining ROIs that overlapped with only one other ROI, both ROIs of an overlapping pair were retained for further analysis only if they overlapped by no more than 5 pixels. Otherwise, only the ROI with the brighter center pixel was retained.

Each selected ROI was then subjected to a nonlinear least-squares estimation to obtain estimates for the expected photon count N_{photon} detected from the Alexa 647 molecule and for the expected per-pixel background photon count β_k (**Supplementary Note 14**). The histogram of the majority of the photon count estimates exhibited an approximately Gaussian distribution. ROIs whose photon count estimate fell outside of this Gaussian distribution (outside the range of 25–350 photons for the LAMP1⁺ cellular structure data set and 50–450 photons for the cell membrane data set) were eliminated from further analysis. Similar elimination

of ROIs was done on the basis of the background estimates, the majority of which also formed an approximately Gaussian distribution. (ROIs with a background estimate outside the range of 0.05–1 photon per pixel in the LAMP1⁺ cellular structure data set, and outside the range of 0.6–1.3 photons per pixel in the cell membrane data set, were discarded.) In total, the eliminations based on the photon count and background estimates resulted in 4.4% and 19.4% of the Alexa 647 spots being discarded, respectively, for the LAMP1⁺ cellular structure and cell membrane data sets.

The Alexa 647 molecules that survived elimination were subjected to maximum-likelihood estimation to obtain the x_0 and y_0 positional coordinates for the construction of the super-resolution image. The localization of each Alexa 647 molecule was performed on a 50 \times 50-pixel ROI extracted from the original, uncompacted image data. The 50 \times 50-pixel ROI was obtained by mapping the pixel coordinates of the molecule's 5 \times 5-pixel ROI back to the pixel coordinates of the original data.

The x_0 and y_0 maximum-likelihood estimates of an Alexa 647 molecule were discarded if they placed the molecule outside of its ROI. Furthermore, estimates were discarded if the function “fminunc” returned an exit flag of <1. The x_0 and y_0 estimates that remained were then corrected for drift as follows. From the data set that was acquired by the reference camera during the acquisition of the super-resolution data, three beads were visually identified from the frames at which the 488-nm activation laser was turned on. For each bead, an ROI centered on its image was extracted from each of the activation frames. (For each bead, the same ROI was in fact extracted from each activation frame, as the drift was not visually detectable.) Each ROI was then subjected to a nonlinear least-squares localization in which the point-spread function model was assumed to be a two-dimensional Gaussian function.

As images acquired by the reference camera were not perfectly spatially aligned with the images produced by the camera that captured the super-resolution data, the resulting x_0 and y_0 estimates for the three beads were multiplied by a transformation matrix to convert their values to the coordinate system of the super-resolution data set. The transformation matrix was determined using a separate data set for which a bead sample was simultaneously imaged by the two cameras. Multiple beads that spanned the field of view of the camera that captured the super-resolution data were chosen, and their ROIs were extracted from the images acquired by each camera and subjected to independent localizations using a nonlinear least-squares estimator in which a Gaussian point-spread function was assumed. The resulting pairs of x_0 and y_0 estimates for each bead were then used to infer the spatial transformation. Specifically, the function “cp2tform” of the MATLAB image processing toolbox was used to obtain a nonreflective similarity transformation matrix.

To determine the drift along the x dimension in the super-resolution data, the transformed x_0 estimates for each of the three reference camera beads were stored in a vector in order of ascending time, and a nonlinear least-squares optimization was used to globally fit a cubic polynomial to the three vectors corresponding to the three beads. The resulting drift curve was then subtracted from the x_0 maximum-likelihood estimates of the Alexa 647 molecules to correct them for drift. Drift in the y dimension was corrected for in completely analogous fashion.

For the construction of the super-resolution image, the pixel size was chosen to be the effective pixel size of the original data set

(16 nm for the LAMP1⁺ cellular structure data set and ~25.4 nm for the cell membrane data set). The dimensions of the image were also chosen to be the same as those for an original data image (200 × 512 pixels for the LAMP1⁺ cellular structure data; 512 × 512 pixels for the cell membrane data).

The super-resolution image was generated by a simple binning of pixel counts. Specifically, starting with a count of 0 in each pixel of the image, the value of a pixel was incremented by 1 for every (drift-corrected) x_0 and y_0 pair that positions an Alexa 647 molecule within the pixel. For presentation (**Fig. 1b** for the LAMP1⁺ cellular structure data set, **Supplementary Fig. 3** for the cell membrane data set), the super-resolution image was adjusted linearly using the “*imadjust*” function of the MATLAB image processing toolbox with no user-supplied adjustment parameters. A total of 11,593 and 23,721 x_0 and y_0 pairs were respectively used to construct the LAMP1⁺ cellular structure and cell membrane super-resolution images, and these location estimates were, respectively, the result of the analysis of 5,063 and 4,909 data images. The same data images were also summed to produce an image for visual comparison with the super-resolution image. The limits of accuracy computed for each super-resolution data set are given in **Supplementary Table 3**.

Live-cell single-molecule tracking data analysis. To demonstrate tracking with UAIM, ErbB2 receptors moving in the plasma membrane of live BT474 human epithelial cells were imaged using Atto 647N-labeled anti-ErbB2 Fab at a 1,000× magnification, and

a data set was analyzed as follows. Visualization of the data was facilitated by compacting the acquired images by a 10 × 10 binning of the pixels to produce images that appeared as if they were acquired using a standard magnification of 100×. Via the manual scanning of this compacted version of the data in the image viewer of our custom microscopy image analysis software²⁴, the track of an Atto 647N molecule was identified by eye. In each of the compacted track frames, a 5 × 5-pixel ROI was manually centered on the tracked Atto 647N spot using a tool that is part of the same custom software environment as the image viewer. Maximum-likelihood localization of the tracked molecule in each frame was then carried out on a 50 × 50-pixel ROI from the original, uncompacted image data, obtained by mapping the pixel coordinates of the 5 × 5-pixel ROI back to the pixel coordinates of the original data. The resulting x_0 and y_0 coordinates were used to generate the track shown in **Figure 1c** and **Supplementary Video 1**, and the associated limits of accuracy are given in **Supplementary Table 3**.

19. Ades, E.W. *et al.* *J. Invest. Dermatol.* **99**, 683–690 (1992).
20. Zheng, W. & Zhao, Q. *Brain Res.* **958**, 371–380 (2002).
21. Born, M. & Wolf, E. *Principles of Optics* 7th edn. (Cambridge University Press, 1999).
22. Ram, S., Ward, E.S. & Ober, R.J. *Multidimens. Syst. Signal Process.* **17**, 27–57 (2006).
23. Olivo-Marin, J.C. *Pattern Recognit.* **35**, 1989–1996 (2002).
24. Chao, J., Ward, E.S. & Ober, R.J. *IEEE Trans. Inf. Technol. Biomed.* **14**, 1075–1087 (2010).